# Evolution of the single-mode Rayleigh-Taylor instability under the influence of time-dependent accelerations

P. Ramaprabhu, V. Karkhanis, R. Banerjee, H. Varshochi, M. Khan, and A. G. W. Lawrie

Phys. Rev. E **93**, 013118 — Published 15 January 2016

DOI: 10.1103/PhysRevE.93.013118

# The Evolution of the single-mode Rayleigh-Taylor instability under the influence of time-dependent accelerations

**P. Ramaprabhu[1], V. Karkhanis[1], R. Banerjee[2], H. Varshochi[1], M. Khan[3], and A.G.W. Lawrie[4]**

**[1]University of North Carolina at Charlotte, Charlotte, NC 28223**
**[2]St. Paul's Cathedral Mission College, Kolkata, India**
**[3]Dept. Instrumentation Science, Jadavpur University, Kolkata, India**
**[4]University of Bristol, United Kingdom**

From nonlinear models and direct numerical simulations we report on several new findings of relevance to the single-mode Rayleigh-Taylor (RT) instability driven by time-varying acceleration histories. The incompressible, Direct Numerical Simulations (DNS) were performed in two- and three-dimensions, and at a range of density ratios of the fluid combinations (characterized by the Atwood number). We investigated several acceleration histories, including acceleration profiles of the general form $g(t) \sim t^n$, with $n \geq 0$ and acceleration histories reminiscent of the Linear Electric Motor experiments. For the 2D flow, results from numerical simulations compare well with a 2D potential flow model and solutions to a Drag-Buoyancy model reported as part of this work. When the simulations are extended to three dimensions, bubble and spike growth rates are in agreement with the so-called level 2 and level 3 models of Mikaelian (PRE 79, 065303, 2009), and with corresponding 3D drag buoyancy model solutions derived in this article. Our generalization of the RT problem to study variable g(t) affords us the opportunity to investigate the appropriate scaling for bubble and spike amplitudes under these conditions. We consider two candidates, the displacement Z and width $s^2$, but find the appropriate scaling is dependent on the density ratios between the fluids – at low density ratios, bubble and spike amplitudes are explained by both $s^2$ and Z, while at large density differences the displacement collapses the spike data. Finally, for all the acceleration profiles studied here, spikes enter a free-fall regime at lower Atwood numbers than predicted by all the models.

## 1. INTRODUCTION:

A material interface demarcating fluids of dissimilar densities is unstable to the Rayleigh[1]-Taylor[2] instability, when an acceleration is applied from the light fluid to the heavy. The fluid mixing resulting from this flow has gained wide attention over the last few decades owing to its role in limiting the performance of Inertial Confinement Fusion capsules[3]. Similarly, RT-driven mixing is essential to explaining transport processes in the detonation of type IA supernovae[4-6], mantle convection[7], formation of volcanic islands[8-10], and density inversions in the upper atmosphere[11]. In ICF, ablation and blow-off at an outer layer results in the shell interface accelerated radially inward with a complex g(t), so that imposed perturbations will grow dominated by a strong RT instability[3]. While the RT-dominated flow in these examples is turbulent and highly nonlinear, a detailed understanding of such flows must be built from a description of the corresponding elemental, single-scale problem [12-20]. For an initially sinusoidal, interfacial perturbation characterized by a perturbation amplitude ($h_0$) and wavenumber k (≡ 2π/λ), linear theory[1-2,21] predicts exponential growth according to:

$$h(t) = h_0 \cosh(\Gamma t), \tag{1}$$

where $\Gamma = \sqrt{Akg}$, with the Atwood number $A \equiv \frac{\rho_b - \rho_a}{\rho_b + \rho_a}$ ($\rho_b > \rho_a$) and a constant g. In reality, the acceleration g can result from a multitude of dynamic phenomena, and vary with time, as observed in applications. Equation (1) is valid for inviscid flows, and only as long as kh(t) << 1. When the perturbation amplitudes evolve to an extent that this condition is violated, the flow may be termed nonlinear. During this stage, the flow is characterized by 'bubbles' of light fluid, and 'spikes' of heavy fluid, although the distinction is significant only at large A when spikes are longer than bubbles. Thus, the nonlinear RT growth is marked by a prolonged phase during which bubble- and spike-tips are observed to advance at a constant velocity given by:

$$V_{b/s} = \sqrt{\frac{2Ag}{(1 \pm A)k}} \ . \tag{2}$$

Note that the above equation implies a constant Froude number for bubble/spike structures given by,

$$Fr_{b/s} = \frac{V_{b/s}}{\sqrt{\frac{Ag\lambda}{(1+A)}}} \ . \tag{3}$$

Equation (2) may be obtained from a potential flow analysis[15,22-27], by choosing appropriate velocity potential functions for the light and heavy fluids which are then substituted in the Bernoulli equation and solved with appropriate boundary conditions. Instead, these results may also be independently obtained from a simple and intuitive accounting of the drag, buoyancy and inertial forces in the flow[26,28-32], using the so-called drag-buoyancy models (DBM).

Thus far, a significant portion of the effort to explain RT flows have been devoted to the limiting case when g = constant. Unfortunately, the situation encountered in experiments and applications

is often more complicated, and may be appropriately described with a time-dependent acceleration history. In ICF, for instance, it is well known that the implosion is characterized by periods of time-dependent acceleration histories[33]. Several studies have sought to exploit the transient behavior arising from complex accelerations to improve capsule performance by more careful profiling of the acceleration pulse. Transients in acceleration histories are also inherent in many experiments[34-37] either by design or by accident, so that their effect on the underlying flow must be quantified to fully understand the flow observed in these experiments. Motivated by these considerations, several recent studies have explored the properties of RT mix driven by complex g profiles. Experimental efforts to investigate variable-g RT have been diverse, and include the rocket rig experiments of [36], the linear electric motor (LEM) experiments[34-35], and the drop-tank experiments of [37-39]. In their analysis of nonlinear RT, Shvarts et al.[28] obtained asymptotic velocities and simple scaling relations for single-mode and multimode RT for A = 1, and under acceleration histories that can be modeled as ~ $t^n$. For the multimode problem, Ramshaw[40] used a wavelength renormalization approach to extend a kinetic energy equation derived for the linear stage to the nonlinear phase of the variable-g RT flow. Finally, Llor[41] compared single-fluid and two-fluid models using so-called self-similar variable acceleration RT (SSVART) as a test case.

We briefly summarize recent models of single-mode RT with g = g(t), before a detailed description of our simulation results in § 4. For a generalized acceleration drive g(t), the linear perturbation growth still follows

$$\ddot{h} - Ag(t)kh = 0 \qquad (4)$$

Mikaelian[42-44] provides analytical solutions to eq. (4) for specific functional forms of g(t). For the late-time nonlinear growth, [43] proposes four models, which are labeled levels 1 – 4 in the order of decreasing complexity (and increasing ease of obtaining analytical solutions). Thus, a level 1 model includes all physics embedded in the Euler equations, but solutions can only be obtained numerically. A level 2 model follows the approach of Layzer[22] and others[27] in defining carefully chosen velocity potential functions for the light and heavy fluids, thus simplifying the governing equations to ODEs. The complete set of equations is provided in [27,43] and not reproduced here, but we note that despite this simplification, an analytical solution cannot be obtained except for special cases. In this paper, we derive our own version of a “level 2 model”, which is valid only for 2D and is compared with our numerical simulations in that limit. A level 3 model, following the work of Mikaelian [42-44], transforms a set of level 2 ODEs of the linear form of (4) into a rescaled variable $\theta_L$ that can be applied to the nonlinear development. A particular value for the initial perturbation $h_0 = 1/(k(1+c))$ must be assumed, and this yields:

$$\ddot{\theta}_L - A_L k_L g(t)\theta_L = 0 \qquad (5)$$

with

$$k_L \equiv \frac{c(1+c)(1+A)k}{2(1+c+cA-A)},$$

$$A_L \equiv \frac{2A}{1+c+cA-A},$$
$$\theta_L \equiv e^{(h-h_0)k_L},$$

and c = 1(2) indicating 3D(2D) flows. Since in these level 3 models, both linear (4) and nonlinear (5) development have the same form, it is possible to establish closed-form analytic solutions for various acceleration profiles [42,43]. While these solutions are strictly valid only for the special value of $h_0$ = 1/(k(1+c)), Mikaelian observes that in practice, this model agrees with the more sophisticated level 3 model over a wide range of initial amplitudes. From our own numerical simulations described in § 4, we agree with this assertion. Finally, [43] also includes a level 4 model, which is obtained by introducing $s \equiv \int_0^t \sqrt{g(t)}\, dt$ so that equation (5) is transformed to a simpler ODE (for certain g(t)s), with solutions of the form $\theta_L = cosh\left(s\sqrt{k_L A_L}\right)$, in analogy with equation (1). We do not include this model in our comparison.

We also compare our 3D simulation results with a drag buoyancy model (DBM), modified by [45] to account for g = g(t). We derive analytic solutions to the DBM in § 2.2, which are compared with the results from our 2D and 3D DNS calculations. In [45], Srebo et al. extend the drag-buoyancy model[28-32] to include time-dependent accelerations, and finite density ratios, resulting in the following set of ODEs for bubble and spike velocities:

$$(\rho_a + C_a\rho_b)\frac{dV_b}{dt} = (\rho_b - \rho_a)g(t) - C_d\rho_b\frac{V_b^2}{\lambda} \qquad (6)$$

$$(\rho_b + C_a\rho_a)\frac{dV_s}{dt} = (\rho_b - \rho_a)g(t) - C_d\rho_a\frac{V_s^2}{\lambda}. \qquad (7)$$

In eqs. (6) - (7), $C_a$ = 2(1) for 2D(3D), while $C_d$ = 6π(2π) for 2D(3D), respectively. Thus, the term on the left represents inertia (with the appropriate added mass), while the terms on the right hand side of each equation represent buoyancy and drag forces, respectively. Furthermore, note that the above equations are valid asymptotically, once artefacts associated with initial conditions decay away. For experiments and simulations initialized with finite sized perturbations, the initial exponential growth of imposed modes must also be included, so that the DB equations are modified as suggested by [45]:

$$\left((C_aE(t)+1)\rho_a + (C_a + E(t))\rho_b\right)\frac{dV_b}{dt} = (1-E(t))(\rho_b - \rho_a)g(t) - C_d\rho_b\frac{V_b^2}{\lambda} \qquad (8)$$

$$\left((C_aE(t)+1)\rho_b + (C_a + E(t))\rho_a\right)\frac{dV_s}{dt} = (1-E(t))(\rho_b - \rho_a)g(t) - C_d\rho_a\frac{V_s^2}{\lambda}. \qquad (9)$$

Thus, the linear RT growth is modeled here through $E(t) = e^{-C_e kh(t)}$, with $C_e$ = 3(2) for 2D(3D) flows. For kh(t) << 1, we recover eq. (4) for time-dependent acceleration histories.

Our objectives in this article are (1) to develop a potential flow model for variable g RT in 2D (§2.1), and to obtain analytical solutions to the DBM for single-mode, RT with g(t) in 2D and 3D (§2.2), (2) to perform detailed 2D and 3D DNS to rigorously validate our potential flow model as well as the closed form solutions developed for the DBM over a wide range of time-dependent profiles, and (3) to use DNS to systematically identify the limits of validity of the potential flow model and the DBM for variable g RT. The rest of the article is organized as follows: In § 2.1, we

derive a Layzer-type 2D potential flow model valid for variable g RT. This is followed by a development of analytical solutions to the DBM in § 2.2, valid for acceleration profiles that satisfy $\frac{\dot{g}}{g^2} \to 0$. The details of the numerical method, problem description, and code validation and numerical convergence study are provided in § 3. In section 4.1, we compare 2D numerical simulations at A = 0.15 and A = 0.9 with the potential flow model described in § 2.1 and the solution to the DBM given in § 2.2. The results are extended to 3D flows in § 4.2 – 4.4. In particular, § 4.2 describes results from simulations at A = 0.15, while the corresponding spike behavior from high Atwood simulations are highlighted in § 4.3. A detailed Atwood variation study was conducted, and is summarized in § 4.4.

## 2. NONLINEAR MODELS

### 2.1. POTENTIAL FLOW MODEL

In this section, we derive a simple potential flow model for variable g RT flows in 2D, and valid for low density ratios of the two fluids. The model may be considered a special case of the generalized Layzer model of [27] valid for 2D flows, and is included here to guide insights in to our simulation results. The derivation of the model follows a Layzer-type framework, later adopted by Goncharov[25] (for arbitrary density ratios) and Mikaelian[42-43] (for variable accelerations in 3D). Following [22-27,46], we define in 2D a perturbation function given by

$$z = \eta(x,t) = \eta_0(t) + \eta_2(t)x^2, \tag{10}$$

where the acceleration g(t) is directed in the negative z-direction, and $\eta_0(t)$ and $\eta_2(t)$ are the time-dependent amplitude and curvature near the bubble tip. Note that for bubbles, $\eta_0 > 0$, and $\eta_2 < 0$, while reversing the signs of these quantities produces incorrect results for spikes, as noted by [42-43], and will not be attempted here. Thus, the potential flow model derived below is only valid for bubbles and spikes in the limit of low Atwood numbers, and for bubbles only in the single-fluid limit (A→ 1). The following velocity potentials are defined for dense and light fluids according to

$$\varphi_h(x,z,t) = a_1(t)\cos(kx)\, e^{-k(z-\eta_0(t))},\ z > 0 \tag{11}$$

$$\varphi_l(x,z,t) = b_0(t)z + b_1(t)\cos(kx)e^{k(z-\eta_0(t))},\ z < 0 \tag{12}$$

where $a_1(t)$, $b_0(t)$ and $b_1(t)$ are the perturbed velocity amplitudes for the heavy and light fluids respectively. To determine the unknown functions $\{\eta_0(t),\eta_2(t),a_1(t),b_0(t),b_1(t)\}$, we resort to stipulating the following kinematic and dynamic boundary conditions.

We first turn to the kinematic conditions corresponding to the interfacial surface perturbation represented by eq. (10):

$$\eta_x(v_h)_x - \eta_x(v_l)_x = (v_h)_z - (v_l)_z \tag{13}$$

$$\eta_t + \eta_x(v_h)_x = (v_h)_x. \tag{14}$$

Substituting eqs. (13) – (14) in (10) and for $\left(v_{h(l)}\right)_x = -\frac{\partial \varphi_{h(l)}}{\partial x}$ from eq. (11) and (12), and expanding in powers of the transverse coordinate *x*, neglecting terms O($x^i$) (i ≥ 3), we obtain the following relations equivalent to the above kinematic boundary conditions:

$$\frac{d\xi_1}{dt} = \xi_3 \tag{15}$$

$$\frac{d\xi_2}{dt} = -\frac{1}{2}\left(6\xi_2 + 1\right)\xi_3 \tag{16}$$

$$b_0 = -\frac{6\xi_2}{3\xi_2 - \frac{1}{2}} k a_1 \tag{17}$$

$$b_1 = \frac{3\xi_2 + \frac{1}{2}}{3\xi_2 - \frac{1}{2}} a_1, \tag{18}$$

where $\xi_1 = k\eta_0$, $\xi_2 = \eta_2/k$, $\xi_3 = {k^2 a_1}\Big/{\sqrt{k g_0}}$, and we define $\tau = t\sqrt{k g_0}$. Thus, $\xi_1$ and $\xi_2$ are the non-dimensional amplitude and curvature, while $\xi_3/k$ is the non-dimensional velocity. Finally, the Bernoulli equation governing both fluids is given by

$$-\rho_{h(l)} \frac{\partial \varphi_{h(l)}}{\partial t} + \frac{1}{2}\rho_{h(l)}\left(\nabla \varphi_{h(l)}\right)^2 + \rho_{h(l)} g(t) z = -p_{h(l)} + f_{h(l)}(t). \tag{19}$$

Substituting the dynamical boundary condition $p_h = p_l$ at the interface $z(x,t) = \eta(x,t)$ in eq. (19), we arrive at

$$\rho_h \left[-\frac{\partial \varphi_h}{\partial t} + \frac{1}{2}(\nabla \varphi_h)^2\right] - \rho_l \left[-\frac{\partial \varphi_l}{\partial t} + \frac{1}{2}(\nabla \varphi_l)^2\right] + g(t)(\rho_h - \rho_l) z = f_h - f_l \tag{20}$$

Substituting for $\varphi_h$, $\varphi_l$ from eqs. (11 – 12) in eq. (20), and equating coefficients of $x^2$, we obtain after some lengthy but straightforward algebraic manipulation, the following evolution equation for $\xi_3$:

$$\frac{d\xi_3}{d\tau} = -\frac{N(\xi_2, r)}{D(\xi_2, r)} \frac{\xi_3^2}{(6\xi_2 - 1)} + 2(r-1)\frac{\xi_2(6\xi_2 - 1)}{D(\xi_2, r)} G(\tau) \tag{21}$$

where $r = \rho_h/\rho_l$ and $G(\tau) = g(t)/g_0$,

$$D\left(\xi_2, r\right) = 12(1-r)\xi_2^2 + 4(1-r)\xi_2 + (r+1)$$

$$N\left(\xi_2, r\right) = 36(1-r)\xi_2^2 + 12(4+r)\xi_2 + (7-r).$$

The coupled system of equations (15-18, 21) can be numerically integrated with the initial conditions $\xi_1(0) = k\eta_0(0)$, $\xi_2(0) = -(\frac{1}{2})\xi_1(0)$, and $\xi_3(0) = 0$ (starting from rest), to obtain solutions for time-evolving bubble amplitude, curvature and velocity for arbitrary g(t). In § 4.1, we compare results from our 2D DNS calculations, with the solution to eq. (21) for several acceleration functions.

### 2.2. ANALYTICAL SOLUTION TO DB MODEL

Here, we derive an analytical solution for the Drag-Buoyancy equation subject to time-dependent acceleration drives. We rewrite equation (6) as,

$$\frac{dV_b}{dt} + a\, V_b^2 = b g(t), \tag{22}$$

with $$a = \frac{C_d\rho_b}{\lambda(\rho_a+C_a\rho_b)},$$

and $$b = \frac{(\rho_b-\rho_a)}{(\rho_a+C_a\rho_b)}.$$

Note that Eq. (22) is a nonlinear *Riccati equation* [47], and can be solved using the approach outlined below. First, the reduction method is used to transform equation (22) to a 2nd order linear equation [48], by defining variable $u$ so that:

$$V_b = \frac{u\prime}{au}. \tag{23}$$

Combining equations (22) and (23) results in:

$$u^{"} - abg(t) = 0, \tag{24}$$

with initial conditions: $u'(0) = 0$ and $u(0) \neq 0$. Equation (24) is similar to eq. (16) in [42], and hence we follow the same approach outlined in that article. Accordingly, equation (24) is transformed to the variable s:

$$\frac{d^2u}{ds^2} - abu(s) + \frac{1}{2g^2}\frac{dg}{dt}\frac{du}{dt} = 0. \tag{25}$$

In the above equation, following [42] the third term may be neglected for acceleration profiles of the form g ~ $t^n$, n ≥ 0 so that $\frac{\dot{g}}{g^2} \sim 0$ (and for many other profiles considered here). The solution to the simplified equation is then:

$$u = c_1\cosh(\sqrt{ab}\, s(t)), \tag{26}$$

where, $c_1$is a constant. Now, substituting (26) into equation (24), we can obtain for the time-dependent, asymptotic bubble velocity $V_b$:

$$V_b = \sqrt{\frac{b}{a}}\frac{ds}{dt}\tanh(\sqrt{ab}\, s(t)) \tag{27}$$

where, $\frac{ds}{dt} = \sqrt{g(t)}$. Note that the asymptotic expression for the bubble Froude number (for both 2D and 3D) may be obtained from (27) as,

$$\frac{V_b}{\sqrt{bg(t)/a}} = \frac{V_b}{\sqrt{2Ag(t)\lambda/C_d(1+A)}} = Fr_b = tanh\left(\sqrt{ab}s(t)\right), \tag{28}$$

with $C_d$ = 6π(2π) for 2D(3D) flows. Eqs. (27) and (28) imply bubble amplitudes that asymptotically evolve as $\ln(\cosh\left(\sqrt{ab}s(t)\right)$, which is the same form of the amplitude solution obtained by [42-43] from his WKB approximation of the potential flow model. This agreement is not surprising, since the Layzer-type potential flow models simplify to the DBM equations at late-times (as originally remarked by [26]). For $g(t) = g_0t^n$, the final equation for $V_b$, will be of the form:

$$V_b = \sqrt{\frac{g_0b}{a}}\, t^{n/2}\tanh(\sqrt{g_0ab}\,\frac{t^{n/2+1}}{n/2+1}). \tag{29}$$

The above procedure is equally valid for spikes, which follow an equation similar to (22), but with

$$a = \frac{C_d\rho_b}{\lambda(\rho_b+C_a\rho_a)},$$

and $$b = \frac{(\rho_b-\rho_a)}{(\rho_b+C_a\rho_a)}.$$

Thus, the spike solution is also given by eq. (27) – (28), but with appropriate modifications for a and b.

Since our numerical simulations were initialized with a finite amplitude, and evolve through a stage of linear growth before culminating in nonlinear saturation, we include a solution to the DBM equations that captures these initial transients. In particular, the bubble and spike amplitudes are particularly sensitive to these transients associated with the linear growth, and the comparison with simulation data will be affected by it. Thus, we integrate the truncated version of eq. (25) not from t = 0, but from t = $t_{nl}$, the transition time from linear to nonlinear RT behavior, when the bubble velocity has reached $V_{b,nl}$, the velocity at the end of linear growth that satisfies the Fermi condition. Upon algebraic simplification, the finite-amplitude counterpart of (27) is obtained as

$$V_b = \sqrt{\frac{bg(t)}{a}}\frac{ce^{2\sqrt{ab}s(t)}-1}{ce^{2\sqrt{ab}s(t)}+1}, \tag{30}$$

where c is obtained from the initial condition $V_b(t_{nl}) = V_{b,nl}$ as

$$c = \frac{1+{}^{V_{b,nl}}/_{f}}{y\left(1-{}^{V_{b,nl}}/_{f}\right)},$$

with $y = e^{2\sqrt{ab}s(t_{nl})}$, $f = \sqrt{\frac{bg(t_{nl})}{a}}$, and $s(t_{nl}) = \int_0^{t_{nl}} \sqrt{g(t)}\, dt$. To compare with our simulation data, we use linear theory solutions for different g-profiles from [42] – [43], as long as kh(t) < 1 ($0 \leq t < t_{nl}$). For larger kh(t), we switch to eq. (30) which is integrated in time to obtain the bubble amplitudes that are used for comparison with the simulation data.

### 3. NUMERICAL METHODS AND PROBLEM SETUP

The DNS calculations described in this article were performed using MOBILE[49-50], a parallelized, 3D variable density, finite volume incompressible flow solver. The advection algorithm is of 3rd order accuracy and - where necessary - preserves monotonicity at every time-step using a nonlinear, upwind-biased numerical scheme. When viscous terms are adequately resolved, there are no regions of the flow where velocity gradients are large relative to the mesh resolution, and thus the nonlinearity of the advection scheme is negligible everywhere and the simulation is truly DNS. The simulations in this article are initialized with a sharp density interface, and in this spatially local and temporally brief instance nonlinearity ensures that the algorithm remains stable. A fractional step approach is employed to incorporate source terms, viscous terms and the pressure correction/velocity projection. Note that the use of multigrid acceleration allows for an efficient solve of the pressure Poisson equation that arises from the projection. Parallelization is implemented through the MPI protocol, while post-processing of flow fields, calculating derived quantities, and reducing them to concise statistics is performed using a macro-language interpreter with a syntax that is transparent to the parallelization. Further details of the advection algorithm available in MOBILE can be found in [49-51].

The single-mode simulations were initialized with sinusoidal perturbations of the interface separating light and heavy fluids, of the form

$$h(x,y) = h_0(\cos(kx) + \cos(ky)), \tag{31}$$

where $h_0$ is the initial perturbation amplitude and $k \equiv 2\pi/\lambda$ is the perturbation wavenumber. For all the simulations described below, we set $h_0$ as 1% of the perturbation wavelength $\lambda$ so that the initial stages of flow development are completely described using the linear theory framework. The dimensions of the computational domain were chosen to be $\lambda$ x $\lambda$ x $\phi\lambda$ in the (x,y,z) directions, where $\lambda$ = 1 cm, and the aspect ratio $\phi$ = 4(8) for low(high) Atwood calculations. Furthermore, for high Atwood number simulations, the initial interface was positioned asymmetrically at z = 2$\lambda$ to allow for the accelerated growth of spikes expected at such large density differences. For the simulations with different time-dependent g-profiles, we maintain a constant value of the scaled kinematic viscosity $\vartheta_{SCL} = \vartheta(t) \Big/ \sqrt{Ag(t)\lambda^3} = 10^{-3}$, thus ensuring the simulations are evolving under the same Reynolds number history regardless of the driving acceleration functions. Since, several of our g-profiles are ~ $t^n$ with n > 0, a constant viscosity (independent of g) would modify growth in the early stages for different g-profiles, thus complicating the comparison of the nonlinear stages which is our main interest in this work. Furthermore, by requiring $\vartheta \sim \sqrt{Ag(t)}$, we ensure that the Reynolds number associated with the secondary Kelvin-Helmholtz instabilities that appear in the nonlinear stage of RT development is the same for all accelerations considered here. Finally, periodic boundary conditions were enforced in the homogeneous directions (x,y), while outflow conditions were imposed on the boundaries along z (direction of gravity).

A detailed grid convergence study was performed with an acceleration profile specified according to $g(t) = g_0(1+\gamma t^2)$, suggested by [42]. Mikaelian[42] derived solutions to the above 'harmonic oscillator' profile, obtained in terms of Hermite polynomials. However, for the special case of $\sqrt{g_0 kA/\gamma} = 1$, the solution for the linear stage reduces to[42,52]

$$h(t) = h_0 e^{\frac{\gamma t^2}{2}} \tag{32}$$

In figure 1(a), we compare the time evolution of the perturbation amplitude from simulations with mesh zoning varied from 8 zones/$\lambda$ to 256 zones/$\lambda$ with eq. (32). We find that for kh(t) < 1 (linear stage RT), simulations with numerical resolution greater than 32 zones/$\lambda$ are in good agreement with the analytical result. At larger amplitudes, the perturbation amplitudes from the numerical simulations undergo nonlinear saturation, and as a result deviate from the exponential growth predicted by equation (32). The corresponding scaled growth rates ($\Gamma/\Gamma_{theory}$) from the linear stage are plotted in figure 1(b) as a function of the normalized zoning parameter k$\Delta$, where $\Delta$ is the mesh spacing in cm. As k$\Delta \rightarrow 0$, the growth rates from the simulations saturate to ~ 90% of the

inviscid theoretical value, with the 10% difference in growth rate likely due to the inclusion of viscosity in the simulations. Table 1 contains a summary of all acceleration profiles included in this study, and their properties.

At the resolution employed in our simulations, we do not expect the numerical viscosity to significantly affect our results in the linear or nonlinear regimes. From dimensional analysis [51 and references therein], the numerical viscosity may be modeled as $\vartheta_{numerical} = \varpi\sqrt{Ag(t)\Delta^3}$, where $\Delta$ = $\lambda$/N is the zone width employed in the simulations, and $\varpi$ is a constant that characterizes the dissipative lossiness of a particular numerical scheme or its implementation. From detailed zoning studies reported in [51], we found $\varpi$ ~ 0.3 for the third order advection implementation in MOBILE. Then, the ratio of physical and numerical viscosities in our simulations could be estimated as $\frac{\vartheta_{physical}}{\vartheta_{numerical}} \sim \frac{\vartheta_{SCL}}{\varpi}\sqrt{\frac{\lambda^3}{\Delta^3}} = \frac{\vartheta_{SCL}}{\varpi}N^{3/2}$ independent of the particular g(t) profile used. For $\vartheta_{SCL}$ ~ $10^{-3}$ and N = 128 zones employed in this work, we estimate $\frac{\vartheta_{physical}}{\vartheta_{numerical}}$ ~ 4.8 so that most of the dissipation observed in our simulations is physical in origin. For the typical simulation parameters employed here, the RT linear growth dispersion relation of [53] may be simplified to $\Gamma \sim \sqrt{Agk} - \vartheta k^2$, by considering g = constant for simplicity and taking $\vartheta^2 k^4 \ll Agk$ for our conditions. Thus, viscous dissipation (physical and numerical) reduces the linear RT growth by an amount $\vartheta k^2$. From figure 1 (b), it can be inferred that the 10% growth reduction observed is primarily due to $\vartheta_{physical}$ which accounts for more than 80% of this reduction in linear growth rate. We expect these trends to continue in to the nonlinear and late-time chaotic stages of RT development. Specifically, the seeding and growth rate of secondary Kelvin-Helmholtz structures is dependent on the viscosity (and Reynolds number), but we expect the physical viscosity to dominate this dynamics as demonstrated above for the linear stage.

## 4. NUMERICAL RESULTS

We first discuss 2D and 3D simulations in this section that were driven by time-dependent acceleration histories of the form $g(t) = g_0 t^n$, with n = 0,1,2,3 and $g_0$ varied for each case so that all simulations evolve to $s^2$ = 200 cm by t = 10 s. For the baseline case (n = 0), this meant $g_0$ = 2 cm/$s^2$. The acceleration history g(t), width $s^2$ , and displacement[34,36] $Z \equiv \int_0^t \int_0^{t"} g(t')dt'dt"$ are plotted for the different acceleration profiles in figures 2 (a), (b) and (c), respectively. Note that the variable Z may be interpreted as the displacement of the test rig in a LEM[34,35]-type of experiment when driven by an acceleration function g(t). For the g(t) profiles shown in figure 2, $\frac{\dot{g}}{g^2} = \frac{n}{g_0}t^{-(n+1)}$ from table 1 and vanishes at late times.

### 4.1 2D SIMULATIONS

To study the effect of dimensionality on the nonlinear RT development under time-varying acceleration histories, we performed a set of 2D DNS calculations initialized with interfacial perturbation specified as $h(x) = h_0 \cos(kx)$, where $h_0 = 0.01\lambda$. We interpret the z-locations of the 1% and 99% planar-averaged volume fraction levels as the bubble and spike tip locations, from which the corresponding amplitudes are inferred. In figures 3 (a) – (c), we plot the time evolution of the bubble/spike amplitudes from 2D simulations with A = 0.15, and $g = g_0 t^n$, with n = 0, 1, and 3, respectively. The data from simulations are compared with the solution from the potential flow model we describe in § 2.1 and the DBM, and show excellent agreement at early and intermediate times ($h_{b/s} < \lambda$). Note that the solution to the potential flow model (Eqs. 15-21) is only valid asymptotically. As a result, the dashed line in figure 3 (a) – (c) is obtained at early times as the solution to the linear theory (eq. 4), while a transition to the nonlinear solution is carried out at $t = t_{nl}$, where $t_{nl}$ can be obtained from the so-called Fermi transition[22]: $\Gamma(t)h(t)_{linear}|_{t=t_{nl}} = V_b|_{t=t_{nl}}$. At late times, the appearance of secondary nonlinear instabilities in the form of Kelvin-Helmholtz (KH) vortices accelerate bubbles and spikes to higher velocities[54-57], in contrast with the "Layzer-type" model which assumes bubble/spike structures where shear instability has not yet developed nonlinearly. The bubble/spike acceleration is particularly evident in figures 4 (a) – (c), where we plot the time development of the Froude number defined in eq. (3), and compare MOBILE results with the potential flow model as well as the analytical solution to the DBM (§ 2.2). The Froude number shows three distinct stages of evolution: (i) an early linear stage, where our simulation results are explained by numerically integrating eq. (4) but for the g(t) profiles considered here, (ii) a nonlinear stage during which the 2D DNS results are in agreement with the DBM and the potential flow model, and (iii) a late-time chaotic stage during which the appearance of Kelvin-Helmholtz vortices complicate the bubble and spike evolution so that the corresponding fronts accelerate away from the constant Froude numbers predicted by the models. In figures 3-4, as n is increased, the linear stage of growth is prolonged in time, but we expect the results to collapse when scaled with either length scales considered here ($s^2$ or Z). This is discussed further in § 4.2.

We repeat these calculations at higher density ratios corresponding to A = 0.9, and plot the corresponding bubble and spike amplitudes in figures 5 (a) – (c). Once again, as n is increased, the amplitude plots reveal a linear growth phase that is extended in time. At such large density differences, the shear-driven Kelvin-Helmholtz instability is inertially suppressed[21,54-55], so that the bubble amplitudes remain in good agreement with the potential flow model even at late times for all the acceleration histories considered here. However, the spike amplitudes in figs. 5 (a) – (c) exhibit accelerated behavior (free-fall) in contrast with the model prediction of a constant terminal velocity. This discrepancy can be clearly seen in the Froude number plots in figs. 6 (a) – (c), where the spike Froude numbers do not show any sign of saturation, in contrast with the 2D

model predictions of an Atwood-dependent Froude number for the spikes. We explore this further for 3D flows in the next section.

### 4.2 3D SIMULATIONS: A = 0.15

**4.2.1 $g(t) = g_0 t^n$:** In this section, we describe results from 3D simulations initialized with perturbations specified according to eq. (31), and at an aspect ratio of 4 (for A = 0.15). Diagonal slices of volume fraction from the simulation with n = 0 are shown in figs. 7 (a) – (c) at early ($t\sqrt{Agk}$ =2), intermediate ($t\sqrt{Agk}$ =6) and late times ($t\sqrt{Agk}$ =8.9) respectively. At early times (fig. 7a), the interface retains its sinusoidal form, while remaining symmetric with respect to the light and heavy fluids. At $t\sqrt{Agk}$ =6, the differentiation of the interface in to bubble and spike structures is evident, while the incipient formation of secondary Kelvin-Helmholtz structures is visible at this stage. By $t\sqrt{Agk}$ =8.9, the KH rollups have saturated to form secondary vortex structures on either side of the primary RT bubble/spike columns. The vorticity associated with the KH instability results in an induced flow that drives the bubble/spike structures to velocities in excess of the potential flow predictions[54-57].

The locations of the bubble and spike fronts (based on displacement from the initial interface height of the 1% and 99% of the planar-averaged volume fraction) are plotted against t in figures 8 (a) – (c) (n = 0, 1 and 3 respectively), while the corresponding Froude numbers are shown in figs. 9 (a) – (c) and compared with the level 2 and 3 models of [43] as well as the modified DBM[45] solution (§ 2.2). The simulations were carried out with $\nu_{SCL} \sim 10^{-3}$, and hence at early times appear to slightly lag behind the models which were initialized with the inviscid linear theory. Following nonlinear saturation, the amplitudes associated with bubble/spike structures are in good agreement with the level 2/3 models[43] as well as the modified DBM[45], while the Froude number from the simulations approaches $1/\sqrt{\pi}$ when scaled by g(t) in eq. (3). Once again, the late-time acceleration due to secondary instabilities is observed for both bubble and spike Froude numbers in figures 9 (a) – (c), but the magnitude of acceleration (and eventual saturation velocity) could be determined by the Reynolds number of the flow[57]. Previous studies[54,57] have observed the precise magnitude of this acceleration could depend on several factors including the viscosity of the flow and the density difference between the fluids.

In fig. 10, we evaluate the appropriate scaling for RT driven by time-dependent g, by plotting the bubble and spike amplitudes against time t (fig. 10 (a)), the width $s^2$ (fig. 10 (b)) and the displacement Z (fig. 10 (c)). From eqs. (6)-(7), it is clear that the use of $s^2$ as a scaling length emphasizes a balance between buoyancy and drag forces in the flow, while the use of 'Z' implies a balance between inertia and buoyancy forces. If either $s^2(t)$ or Z(t) were found to adequately collapse all of our results, it would imply the existence of a universal scaling parameter, and thus a universal solution that describes all acceleration profiles. Models suggest $s^2$ should be that

variable, an assertion we test with our 3D simulations. Furthermore, since $s^2$ and Z emphasize the balance between different aspects of the drag-buoyancy equation, collapsing the data based on either variable would imply the dominance of those terms in the DBM and the flow dynamics. Clearly, neither picture is sufficiently complete when g(t) varies with time, but earlier studies[34,36,42-43] have shown the scaling width $s^2$ collapses bubble (and spike) amplitudes at low Atwood numbers, while spike amplitudes are explained by the displacement 'Z' at large density differences. Furthermore, $s^2$ falls out as a natural length scale in the analytical solutions derived in [43], as well as the solution to the DBM obtained in § 2.2 of this article. In spite of this, for the low Atwood number set plotted in fig. 10, we find both $s^2$ and 'Z' to collapse the amplitudes from all of our simulations with varying values of n. Thus, we defer a judgment on the appropriate scaling for time-dependent g's to the next section, where we examine RT behavior at large density differences.

**4.2.2 LEM-type profiles:** We examine two idealized g-profiles inspired by the Linear Electric Motor experiments of [34,35], and theoretically investigated by Mikaelian[42-43]. The acceleration histories studied here (figure 11 (a)) correspond to an idealization of profiles G_1 and G_2 reported in [34], and are given by

$$g(t) = \frac{g_0}{t_0} t, t \leq t_0 \qquad (33)$$

$$g(t) = g_0 \left\{1 - \frac{t-t_0}{t_L-t_0}\right\}, t > t_0.$$

In figure 11, LEM1(2) profiles correspond to $t_0$ = 2(6), while $g_0$ = 6 cm/s$^2$ and the time of the end of the 'experiment' $t_L$ = 8s for both cases. The corresponding scale $s^2$ is plotted in figure 11 (b) for both profiles, and is given by the expression $s^2(t_L) = \frac{4}{9} g_0 t_L^2$, independent of $t_0$ the time at which the acceleration pivots from positive to negative slope. In contrast, the displacement Z(t) retains a dependence of $t_0$ (Table 1), and is shown for both profiles in figure 11 (c). For the first segment ($\dot{g} > 0$), Mikaelian[43] provides linear theory solutions in terms of Airy functions, which we use to initialize $V_{b,nl}$ in our Drag-Buoyancy model (eq. 30). Eq. (33) may also be easily modified to represent an impulsively accelerated test cell giving rise to a Richtmyer-Meshkov (RM) instability-driven flow, but we have not included this case in our analysis.

Figure 12 (a) and (b) are plots of time evolution of bubble and spike amplitudes for the LEM1 and LEM2 profiles respectively obtained from our 3D DNS calculations. We also include predictions of bubble amplitude from the Level 3 model of [43] and bubble and spike amplitudes from our analytical solution to the DBM equations. Once again, the planar-averaged amplitudes obtained from simulation results are in good agreement with the simplified potential flow solution[43] as well as the DBM solution obtained in § 2. At late times, slight deviation between simulations and models are observed due to the appearance of secondary KH instabilities that accelerate the bubble and spike tips. The solution to the DBM equation asymptotes to a Froude number of ~

$1/\sqrt{\pi}$ for the bubble in agreement with simulation data (0.58 ± 0.04) before secondary instabilities assert themselves on the bubble dynamics. Similarly, the spike Froude number is obtained from eq. (3) as $Fr_s \rightarrow 0.65$ in agreement with our simulation predictions (0.7 ± 0.03). As commented earlier, we find that both scaling widths ($s^2$ and Z) collapse bubble and spike data from the different LEM simulations, with the scale $s^2$ achieving slightly better collapse of the data.

#### 4.2.3 $g(t) = g_0(t/t_0)^a$, a = -1.2:

Acceleration profiles that evolve as $t^a$ with a < 0 are interesting since they violate the condition $\dot{g}/g^2 \rightarrow 0$, required to obtain closed-form solutions to the DBM or the level 4 model of [43]. Thus, such profiles could potentially constitute a discriminating test case for the analytical solutions derived in this work. We report results from 3D simulations driven by

$$g(t) = g_0\left(\frac{t}{t_0}\right)^a, \; t > t_0 \tag{34}$$

$$g(t) = 0, t \leq t_0,$$

with a = -1.2 and $g_0$ = 2 cm/$s^2$. Furthermore, [58,59] attribute blastwave acceleration observed in their experiments on the OMEGA laser to a g-profile modeled by eq. (34), with a ~ -1.2. Recent numerical simulations of a chemically reacting RM mixing layer[60] revealed pressure waves from combustion that accelerated the material interface approximately according to the profiles specified in eq. (34). Figure 13 is a plot of the time dependence of the variables (g, $s^2$, Z) for the acceleration profiles considered in this section. For this acceleration profile, the scaling width $s^2$ and displacement Z for $t > t_0$ are given by

$$s^2 = \left\{\frac{4g_0}{t_0^a(a+2)^2}\left(t^{\frac{a+2}{2}} - t_0^{\frac{a+2}{2}}\right)^2\right\} \tag{35}$$

$$Z = \frac{g_0}{t_0^a(a+1)}\left\{\frac{t^{a+2} - t_0^{a+2}}{a+2} - t_0^{a+1}(t - t_0)\right\} \tag{36}$$

and are thus related through a complex time-dependent expression. In figure 14, we plot bubble and spike amplitudes for the above acceleration history, which show good agreement with predictions from the DBM solution (eq. 30) and the simplified level 3 model from [43], even though $\dot{g}/g^2 \neq 0$ for these profiles. The RT flow is initialized by the impulsive acceleration at $t = t_0$, followed by a decaying function.

### 4.3 3D SIMULATIONS: A = 0.9

The simulations described above were repeated with a fluid density ratio of 19 (A = 0.9), with the perturbation interface positioned asymmetrically at z = 2λ to accommodate spike acceleration. Similar to fig. 7, we plot the diagonal slices of the volume fraction at early, intermediate and late

times for the large Atwood number simulations in figs. 15 (a) – (d). Following nonlinear saturation ($\tau$ = 6), significant asymmetry is visible between bubble and spike structures in figs. 15 (c) and (d), with the spikes outpacing bubble penetration in to the heavy fluid. In contrast with the low Atwood number simulations, secondary instabilities are inertially suppressed at large density differences[21] rendering bubble and spike structures featureless.

The time evolution of planar-averaged bubble and spike amplitudes are shown in figures 16 (a) – (c) for the high A simulations with n = 0, 1, and 3, respectively. The corresponding plots for the bubble/spike Froude numbers are shown in figs. 17 (a) – (c). In fig. 16, the bubble amplitudes are compared with the level 2/3 models of [43] and the modified DBM[45], while the spike amplitudes are compared with the DBM prediction since the potential flow models are not valid for spikes at large density differences. In contrast to the low Atwood results, at A = 0.9, bubble velocity asymptotes at late times with a terminal velocity that is marked by a Froude number $\rightarrow 1/\sqrt{\pi}$ in agreement with eq. (3), and independent of the specific acceleration profile used. Thus, in this limit, the suppression of secondary instabilities renders bubble profiles consistent with the assumptions in potential flow models, which accurately predict the bubble amplitudes/velocities for n = 0, 1, and 3. Figure 17 reveals strikingly different behavior for spikes, which appear to evolve with an acceleration for instance corresponding to $h_s \sim gt^2$ (for n = 0) in agreement with the potential flow model of Zhang [60]. However, note that the model of [61] suggests free-fall behavior for spikes only in the limit of $\rho_h/\rho_l \rightarrow \infty$, while the simulations in this work reveal such a behavior even at finite (but large) density ratios. We explore this trend in greater detail in § 4.4, where we discuss an Atwood variation study. The spike prediction from the modified DBM misses this critical behavior, instead evolving to a saturation Froude number that is dependent on A.

We explore the appropriate scaling behavior at large Atwood numbers by plotting bubble and spike amplitudes against t (fig. 18 a), width $s^2$ (fig. 18 b) and the displacement Z (fig. 18 c). Bubble amplitudes are adequately explained by $s^2$ and Z (figs. 18 (b) – (c)), so that $h_b$ from simulations with different n collapse when plotted against both length scales. However, the collapse for spike amplitudes is significantly improved when plotted against the displacement Z over the width $s^2$. A closer examination of eqs. (7) or (9) confirms this behavior, since $\rho_l \rightarrow 0$ implies vanishing drag and a dynamic balance only between inertia and buoyancy, the balance implied by the displacement Z.

### 4.4 ATWOOD VARIATION STUDY

To elucidate bubble and spike scaling at any density ratio or driving acceleration profile, we performed a set of 3D simulations at A = 0.5 (n=3), 0.6 (n=2), 0.7 (n=1), 0.8 (n=1), 0.9 (n=0), and 0.9 (n=1). Based on the earlier discussion, we restrict ourselves to spike behavior in this section, since bubbles appear to evolve independent of the density ratios (modulo secondary instabilities). We plot $-h_s$ vs t for all the cases considered here in figure 19 (a). From eq. (9) at large density

differences ($\rho_l \rightarrow 0$) and late times ($E(t) \rightarrow 0$), it is reasonable to expect that spikes should evolve with $h_s \sim 2AZ(t)$ or

$$h_s = 2\alpha_s AZ(t). \quad (37)$$

For A = 1, eq. (7) and Zhang[61] predict $\alpha_s = 0.5$, but the behavior at finite density ratios (and time-varying acceleration histories) is not clear. By varying A and n in our simulations, we seek to verify the applicability of eq. (37) over a wide range of conditions. From our detailed simulation study, we find that eq. (37) accurately describes spike behavior for $A \geq 0.5$, while spikes resemble bubbles at lower density ratios. Figure 19 (b) is a plot of the spike acceleration coefficient $\alpha_s$ against the Atwood number from our parameter scan, where $\alpha_s$ is obtained in each case from fitting eq. (37) to our simulation data. In addition to data from MOBILE, we also plot results from earlier studies at constant g (n = 0), including simulations using the incompressible code RTI3D[19,55,62], and the experiments of [18] that used magnetorheological fluids to achieve $A \rightarrow 1$. Regardless of the value of 'n', figure 19 (b) clearly shows spike free fall behavior for $A \geq 0.5$ from both simulations and experiments. This finding lies in contrast to the DBM[28-32,45], as well as the potential flow models[22-27]. In figure 19 (c), we plot the spike amplitudes from all the simulations described above, and find that spikes satisfy $h_s \sim 2\alpha_s AZ(t)$ in every case.

**5 SUMMARY**

Using nonlinear models and 3D Direct Numerical Simulations, we have investigated the response of the single-scale RT problem to time-dependent accelerations. As noted earlier, experiments[17-20,34-36] and applications[3-11] are more suitably characterized by such complex, acceleration histories rather than a constant g, which has been the focus of most RT studies. Several acceleration profiles were considered as part of our study, including profiles that fit $g(t)=g_0t^n$, LEM-type profiles, and g-profiles that are suggestive of blastwaves. Our results build extensively on earlier work by many authors, particularly the series of articles by Mikaelian [42-44], who developed potential flow models (at different levels of coarse-graining) that were compared with 2D simulations using the CALE code. In the current study, we have developed a 2D potential flow model, while also deriving solutions to an intuitive drag-buoyancy model[28-32] for bubble and spike tips for any g-profile satisfying the condition $\frac{\dot{g}}{g^2} \rightarrow 0$. We validate our models with detailed 2D and 3D simulations of variable g RT. By systematically varying the Atwood number, we are able to elucidate spike behavior and clarify limitations of existing potential flow and drag-buoyancy models. Finally, the wide range of acceleration histories and density ratios explored here allows us to investigate appropriate scaling factors for bubble and spike amplitudes. A brief discussion of our results follows.

*Models:* Consistent with earlier findings[42-44], we report bubble amplitudes from 3D simulations in good agreement with predictions from potential flow models as well as the DBM, for all A and g-profiles investigated. We have developed a 2D potential flow model valid for arbitrary g(t), which

we have validated extensively using numerical simulations. We compare bubble amplitudes from 3D MOBILE simulations with the level 2/3 models of [43], and our solutions to the DBM presented in the § 2 (accounting for transients due to the initial linear growth). The DBM solution was obtained by transforming the original set of nonlinear equations (6-7) to a linear, 2nd order equation. Following [42,43], we neglect $\frac{\dot{g}}{g^2}$ to obtain a general analytic solution in terms of the variable s. Note that the omission of the $\frac{\dot{g}}{g^2}$ term was not found to be very restrictive, with the DBM (and likely the level 4 model) successfully predicting the bubble amplitudes for all cases considered here, even when $g \sim t^a$, $a < -1$, which would seemingly violate this condition. From the simulations and models, we conclude bubbles always evolve with a constant Froude number approaching $1/\sqrt{\pi}$.

*Atwood number:* Spikes exhibit a strong dependence on the Atwood number, mimicking bubble behavior at low density differences, while transitioning to free-fall behavior at large A. None of the existing models accurately describe this transition, which occurs at A ~ 0.5 in our simulations. Thus, for $A \geq 0.5$, our simulations suggest $h_s = 2\alpha_s AZ$, where Z is a displacement scale and $\alpha_s$ is an Atwood-dependent growth coefficient for spikes. We find that in general, potential flow models[22-27] are incapable of describing the spike free-fall observed in our simulations occurring at large density ratios, since they do not account for the sharpening of the spike tips. An exception is the Zhang model[61] for 2D spikes that was generalized to 3D in [63], which accurately predicts $\alpha_s = 0.5$ at A = 1 (fluid/vacuum case). Eq. (7) also captures spike behavior at infinite density ratios, since the last term in that equation vanishes in that limit resulting in the expected free-fall behavior. However, several simulations[19,55] including results from MOBILE presented here, have revealed the onset of the so-called "free-fall" behavior to occur starting at A ~ 0.5. If confirmed with experimental verification, this would imply no single model describes the entire range of spike behavior – spike evolution at the extremes in Atwood number are captured by the potential flow models (A→ 0) and the model of Zhang/DBM (A→ 1) respectively, but the transition between these limits remains unexplained by models. Mikaelian[44] has suggested interpolating between the extremes of spike behavior. Such an interpolation strategy will have to be informed by the new simulation results presented here. Alternatively, eq. (7) may be modified by neglecting the drag term for A > 0.5, but an additional coefficient must be introduced to explain the Atwood-dependent growth rate $\alpha_s(A)$.

*Scaling:* Simulations driven by time-dependent accelerations also afford us the opportunity to search for the existence of a universal scaling parameter that collapses bubble/spike amplitudes from any g(t). For instance, the level 4 model of [43] (and our DBM solution) obtain bubble and spike amplitudes as explicit functions of s, rather than the displacement function Z. As noted earlier, the Z-scaling emphasizes a dynamic balance between inertia and buoyancy forces in eq. (6-7), while the $s^2$-scaling implies buoyancy and drag forces are balanced. The width ($s^2$) was

introduced as a candidate for scaling observed amplitudes from the rocket rig experiments[36]. The LEM experiments[34,35] evaluated both variables and concluded that the width provided a slightly better collapse of the turbulent mixing width data. From 2D single-mode simulations, Mikaelian[42,43] also found a better collapse when amplitudes were plotted against $s^2$ rather than Z, but only at low A.

From our detailed simulation study with a wide range of acceleration profiles, and variations in the Atwood number, we conclude there is no single scaling variable that collapses all the reported data. At low A, the solution to the DBM and level 4 models suggest bubbles (and spikes) should prefer to scale with $s^2$. However, an examination of fig. 10 suggests both scaling variables collapse the data reasonably well. This is not surprising since for the acceleration profiles shown in fig. 10 ($g \sim t^n$), $s^2/Z$ is constant and independent of time. This result was derived analytically in [44], and implies both variables encapsulate the same time dependence associated with g(t) and can thus collapse the data equally well for such acceleration histories. In fact, this remained the case for many of the g-profiles investigated in our study (table 1). We also investigated through numerical simulations, acceleration profiles of the form,

$$g(t) = \frac{g_0}{\left(1-\frac{t}{T}\right)^a}, \tag{38}$$

with a = -2 or -3 and t < T. The case a = -2 was investigated by [44], who defined $\tau$ = 1- t/T and obtained the ratio $s^2/Z$ as a strong function of $\tau$. For a = -2, $\frac{s^2}{Z} \sim -\ln\left(1-\frac{t}{T}\right)$ and diverges as t → T, but the solution is self-similar. However for a = -3, $s^2/Z$ is independent of t asymptotically. We compare data from simulations with a = -2 and -3 in fig. 20, and find both $s^2$ and Z to collapse the amplitudes. Finally, we also compared data between different classes of acceleration profiles, and still found both scaling variables to be adequate. It is surprising that even for g-profiles where $s^2/Z$ depends strongly on time, both variables collapse our simulation data. Since the displacement Z also explains our spike data (starting at A > 0.5), these results suggest that Z might be a superior scaling over the entire range of density differences studied here.

At A = 1, the DBM explicitly suggests a scaling of spike amplitudes with the displacement Z (since the drag term in eq. 7 vanishes), while bubbles should retain the same behavior from low A. Data from several previous simulations, experiments, as well as the MOBILE calculations reported in this work support this claim. While potential flow models generally fail in this limit, the model of Zhang[61] and the extension by [63] capture this behavior as well as the observed spike growth rate of $\alpha_s$ = 0.5. However, our simulations report $h_s \sim Z$ (and not $s^2$) for any g-profile, even at finite density ratios, starting at A = 0.5. If verified experimentally, this would require corresponding modifications to both the DBM and the potential flow models. From the above, we conclude for most acceleration profiles that satisfy $s^2/Z$ → constant either exactly or asymptotically, bubbles (at any A) and spikes (at low A) may be collapsed adequately with either scale. For certain profiles[44] that violate this condition (fig. 20), the width should be the superior

scaling, however even in such cases we find the displacement to collapse the data reasonably well. For A > 0.5, spikes from any acceleration grow as $2\alpha_s AZ$, with the growth rate $\alpha_s$ depending on the density ratio.

**ACKNOWLEDGEMENTS:** This work was supported in part by the (U.S.) Department of Energy (DOE) under Contract No. DE-AC52-06NA2-5396. The authors are deeply grateful to Dr. Karnig Mikaelian for extensive discussions and valuable insights that have guided this work.

| $g$ | $s^2 \equiv \left\{\sqrt{g(t)}dt\right\}^2$ | $U \equiv \int g(t)\,dt$ | $Z \equiv \int \left(\int g\,dt\right)dt$ | $\frac{\dot{g}}{g^2}$ |
|---|---|---|---|---|
| $g_0 t^n$ | $\frac{4g_0}{(n+2)^2}t^{n+2}$ | $\frac{g_0}{n+1}t^{n+1}$ | $\frac{g_0}{(n+1)(n+2)}t^{n+2}$ | $\frac{n}{g_0}t^{-(n+1)}$ |
| $g_0(1+\propto t^2)$ | $g_0\left\{\frac{1}{2}t\sqrt{1+\alpha t^2} + \frac{\sinh^{-1}\left(\sqrt{\alpha}t\right)}{2\sqrt{\alpha}}\right\}^2$ | $g_0 t + \frac{1}{3}g_0 \propto t^3$ | $\frac{1}{2}g_0 t^2 + \frac{1}{12}g_0 \propto t^4$ | $\frac{2 \propto t}{g_0(1+\propto t^2)^2}$ |
| $\begin{cases}\frac{g_0}{t_0}t & t \le t_0 \\ g_0\left\{1-\frac{t-t_0}{t_L-t_0}\right\} & t > t_0\end{cases}$ | $\frac{4}{9}\,g_0\left\{t_L - \frac{(t_L-t)^{\frac{3}{2}}}{\sqrt{t_L-t_0}}\right\}^2$, t >$t_0$ | $\frac{g_0}{2(t_L-t_0)}\{-t^2 + 2t_L t - t_L t_0\}$, t > $t_0$ | $\frac{g_0 t_0^2}{6} + \frac{g_0}{2(t_L-t_0)}\left\{-\frac{1}{3}t^3 + t_L t^2 - t_L t_0 t + \frac{1}{3}t_0^3\right\}$, t > $t_0$ | $\begin{cases}\frac{t_0}{g_0 t^2} & t \le t_0 \\ \frac{-(t_L-t_0)}{g_0^2(t_L-t)} & t > t_0\end{cases}$ |
| $\begin{cases}0 & t < t_0 \\ g_0\left(\frac{t}{t_0}\right)^a & t \ge t_0\end{cases}$ $a < -1$ | $\frac{4}{(a+2)^2}\frac{g_0}{t_0^a}\left(t^{\frac{a+2}{2}} - t_0^{\frac{a+2}{2}}\right)^2$, t> $t_0$ | $\frac{g_0(t^{a+1}-t_0{}^{a+1})}{(a+1)t_0^a}$, t > $t_0$ | $\frac{g_0}{(a+1)t_0^a}\left\{\frac{t^{a+2}-t_0^{a+2}}{(a+2)} - t_0^{a+1}(t-t_0)\right\}$, t > $t_0$ | $\begin{cases}\frac{at_0^a}{g_0 t^{a+1}} & t \ge t_0\end{cases}$ |
| $\frac{g_0}{(1-\frac{t}{T})^2}$ | $T^2 g_0\left\{\ln(1-\frac{t}{T})\right\}^2$ | $\frac{g_0 T}{(1-\frac{t}{T})} - g_0 T$ | $-T^2 g_0 \ln\left(1-\frac{t}{T}\right) - g_0 T t$ | $\frac{2}{g_0 T}(1-\frac{t}{T})$ |
| $\frac{g_0}{\left(1-\frac{t}{T}\right)^3}$ | $4T^2 g_0\left\{\frac{1}{\sqrt{1-{}^t/_T}} - 1\right\}^2$ | $\frac{g_0 T}{2(1-\frac{t}{T})^2} - \frac{g_0 T}{2}$ | $\frac{g_0 T^2}{2(1-\frac{t}{T})} - \frac{g_0 T}{2}t - \frac{g_0 T^2}{2}$ | $\frac{3}{g_0 T}(1-\frac{t}{T})^2$ |

Table 1: Summary of acceleration profiles investigated using MOBILE.

**REFERENCES:**


1. Lord Rayleigh, Scientific Papers II (Cambridge University Press, Cambridge, 1900), pp. 200-207.
2. G.I.Taylor, Proc. R. Soc. London, Ser. A **201**, 192 (1950).
3. J.D. Lindl, Inertial Confinement Fusion: The Quest for Ignition and Energy Gain using Indirect Drive (Springer-Verlag, New York, 1998).
4. M. Zingale et al., Astrophys J., **632**, 1021 (2005).
5. M. Herant, W. Benz, W.R. Hix, C.L. Fryer and S.A. Colgate, Astrophys J., **435**, 339 (1994).
6. C.-Y. Wang and R.A. Chevalier, Astrophys J., **549**, 1119 (2001).
7. S. Zhang and M.T. Zuber, Earth and Planetary Sci. Lett., **189**, 75 (2001).
8. B.D. Marsh, J. Geol., **87**, 68 (1979).
9. B.D. Marsh and I.S.E. Carmichael, J. Geophys. Res., **79**, 1196 (1974).
10. S.A. Fedotov, Bull. Volcanologique, **39(2)**, 241 (1975).
11. C.S. Huang, M.C. Kelley, and D.L. Hysell, J. Geophys. Res., 98, 15 (1993).
12. D.J. Lewis, Proc. R. Soc. London, Ser. A., **202**, 81 (1950).
13. R.M. Davies and G.I. Taylor, Proc. R. Soc. London, Ser. A., **200**, 375 (1950).
14. R. Collins, J. Fluid Mech., **28**, 97 (1967).
15. J. Hecht, U. Alon and D. Shvarts, Phys. Fluids, **6**, 4019 (1994).
16. J. Hecht, D. Offer, U. Alon, D. Shvarts, S.A. Orszag and R.L. McCrory, Laser Part. Beams, **13**, 423 (1995).
17. J.P. Wilkinson and J.W. Jacobs, Phys. Fluids, **19**, 124102 (2007).
18. J. White et al., Phys. Rev. E., **81**, 026303 (2010).
19. P. Ramaprabhu and G. Dimonte, Phys. Rev. E., **71**, 036314 (2005).
20. D.H. Sharp, Physica D., **12**, 3 (1984).
21. S. Chandrasekhar, Hydrodynamic and Hydromagnetic Stability (Oxford University Press, Oxford, 1961).
22. D. Layzer, Astrophys J., **122**, 1 (1955).
23. S.I. Sohn, Phys. Rev. E., **67**, 026301 (2003).
24. S. Abarzhi et al., Phys. Lett., A **317**, 470 (2003).
25. V.N. Goncharov, Phys. Rev. Lett., **88**, 134502 (2002).
26. U. Alon, J. Hecht, D. Ofer and D. Shvarts, Phys. Rev. Lett., **74**, 534 (1995).
27. K.O. Mikaelian, Phys. Fluids, **21**, 024103 (2009).
28. D.Shvarts, U.Alon, D. Ofer, R.L. McCrory and C.P. Verdon, Phys. Plasmas, **2**, 2465 (1995).
29. G. Dimonte, Phys. Plasmas, **7**, 2255 (2000).
30. B. Cheng, J. Glimm and D.H. Sharp, Phys. Rev. E., **66**, 036312 (2002).

31. Y.G. Cao, W.K. Chow and N.K. Fong, Comm. Theor. Phys., **56**, 751 (2011).
32. S. Bouquet, P. Gandeboeuf and Pierre Pailhories, Math. Meth. Appl. Sci., **30**, 2027 (2007).
33. R. Betti et al., Phys. Rev. Lett., **98**, 155001 (2007).
34. G. Dimonte and M. Schneider, Phys. Fluids, **12(2)**, 304 (2000).
35. G. Dimonte and M. Schneider, Phys. Rev. E., **54**, 3740 (1996).
36. K.I. Read, Physica D., **12**, 45 (1984).
37. J.W. Jacobs and J.M. Sheeley, Phys. Fluids, **8**, 405 (1996).
38. C.E. Niederhaus and J.W. Jacobs, J. Fluid Mech., **485**, 243 (2003).
39. P. R. Chapman and J.W. Jacobs, Phys. Fluids, **18**, 074101 (2006).
40. J.D. Ramshaw, Phys. Rev. E., **58**, 5834 (1998).
41. A. Llor, Laser and Part. Beams, **21**, 305 (2003).
42. K.O. Mikaelian, Phys. Rev. E.,**79**, 065303(R) (2009).
43. K.O. Mikaelian, Phys. Rev. E., **81**, 016325 (2010).
44. K.O. Mikaelian, Phys. Rev. E., **89**, 053009 (2014).
45. Y. Srebro, Y. Elbaz, O. Sadot, L. Arazi and D. Shvarts, Laser and Part. Beams, **21**, 347 (2003).
46. Banerjee, R., Mandal, L., Roy, S., Khan, M., and Gupta, M.R., Phys. Plasmas, **18**, 022109 2011.
47. Reid, William Thomas. Riccati differential equations. Elsevier, 1972.
48. Ince, Edward Lindsay. Ordinary Differential Equations. Dover Publications, 1956.
49. A.G.W. Lawrie, “On Rayleigh-Taylor mixing: confinement by stratification and geometry”, Ph.D. Thesis (University of Cambridge, 2009).
50. A.G.W. Lawrie and S.B. Dalziel, Phys. Fluids, **23**, 085109 (2011).
51. P. Ramaprabhu, V. Karkhanis and A.G.W. Lawrie, Phys. Fluids, **25**, 115104 (2013).
52. K.O. Mikaelian, Private Communication.
53. S.I. Sohn, Phys. Rev. E., **80**, 055302(R) (2009).
54. P. Ramaprabhu et al., Phys. Fluids, **24**, 074107 (2012).
55. P. Ramaprabhu et al., Phys. Rev. E., **74**, 066308 (2006).
56. J. Glimm, X.L. Li and A.-D. Lin, Acta Math. Appl. Sin.,**18**, 1 (2002).
57. T. Wei and D. Livescu, Phys. Rev. E., **86**, 046405, (2012).
58. C.C. Kuranz et al., Astrophys. J., **696**, 749, (2009).
59. R.P. Drake et al., Phys. Plasmas, **11(5)**, 2829 (2004).
60. N. Attal and P. Ramaprabhu, Shock Waves, **25(3)**, 1, (2015).
61. Q. Zhang, Phys. Rev. Lett., **81**, 3391 (1998).
62. M.J. Andrews, Int. J. Numer. Meth. Fluids, **21**, 205 (1995).
63. K.O. Mikaelian, Phys. Rev. E., **78**, 015303(R) (2008).

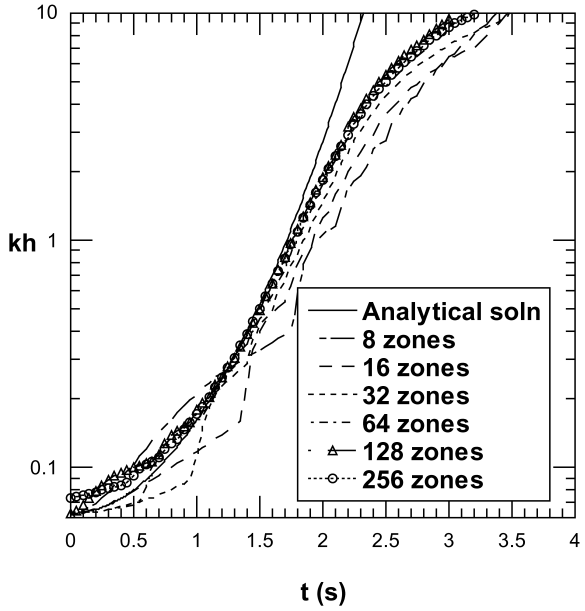


(a)

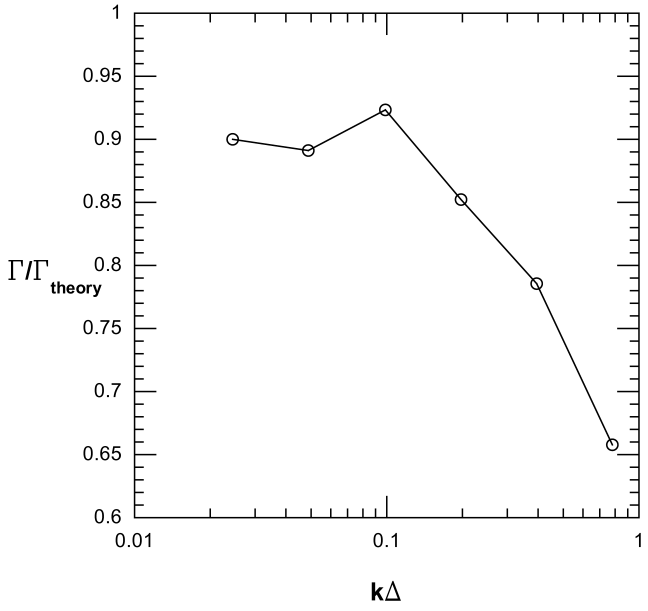


(b)

Figure 1 EE11392 15DEC2015

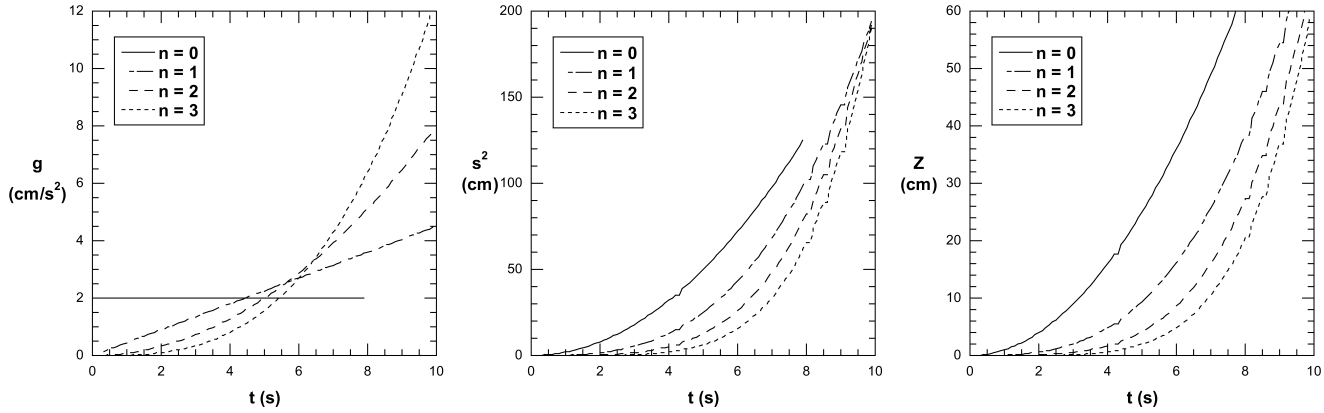


Figure 2 EE11392 15DEC2015

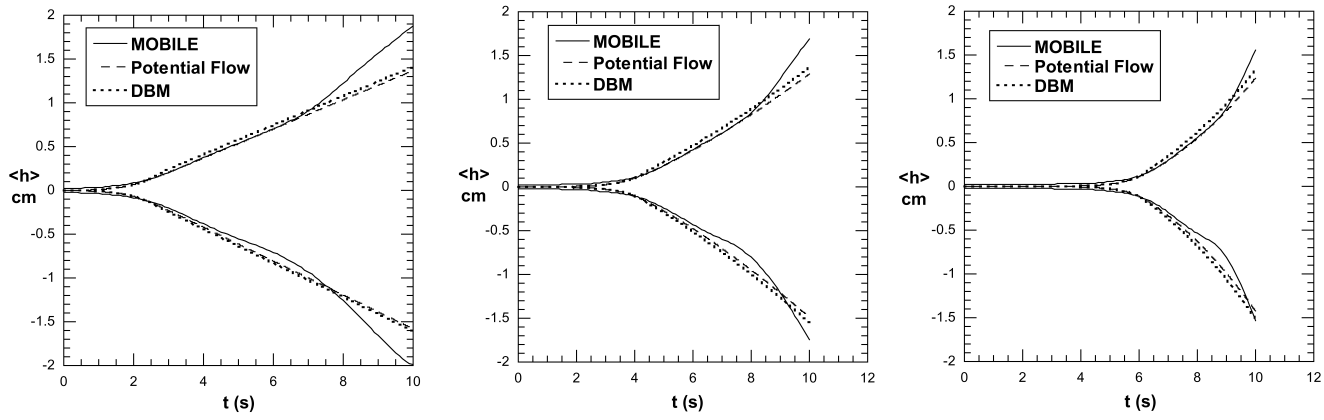


Figure 3 EE11392 15DEC2015

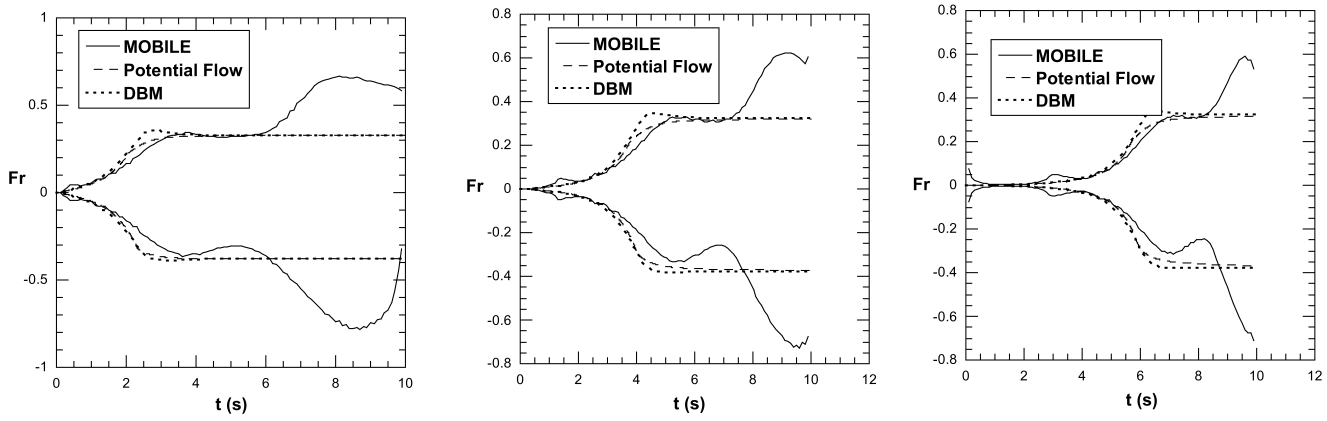


Figure 4 EE11392 15DEC2015

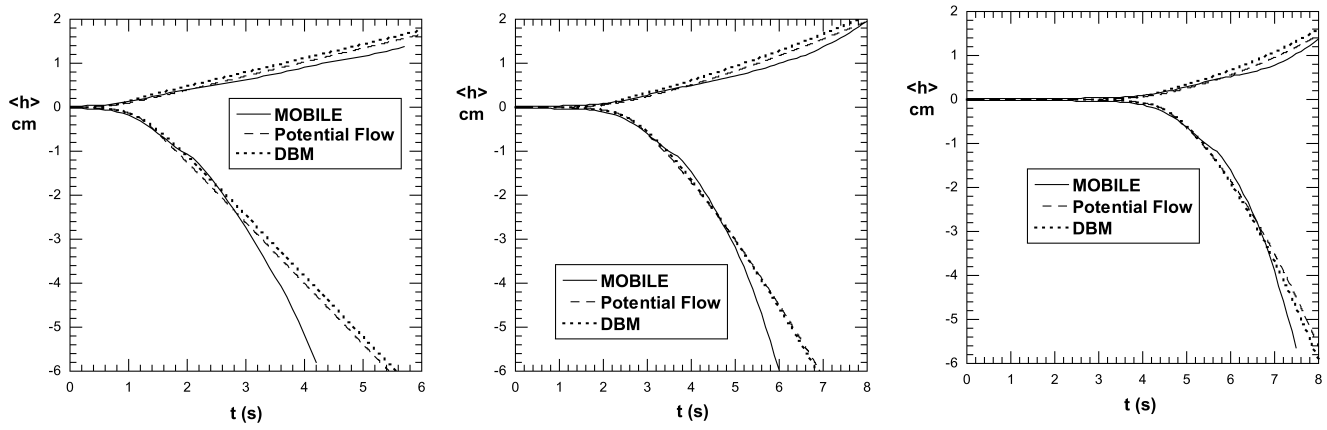


Figure 5 EE11392 15DEC2015

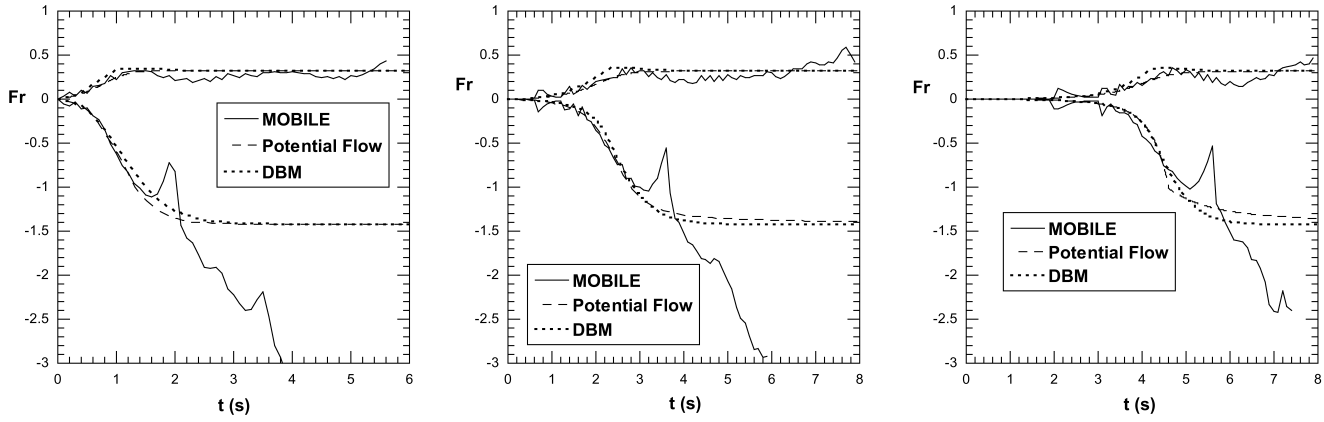


Figure 6 EE11392 15DEC2015


Figure 7 EE11392 15DEC2015

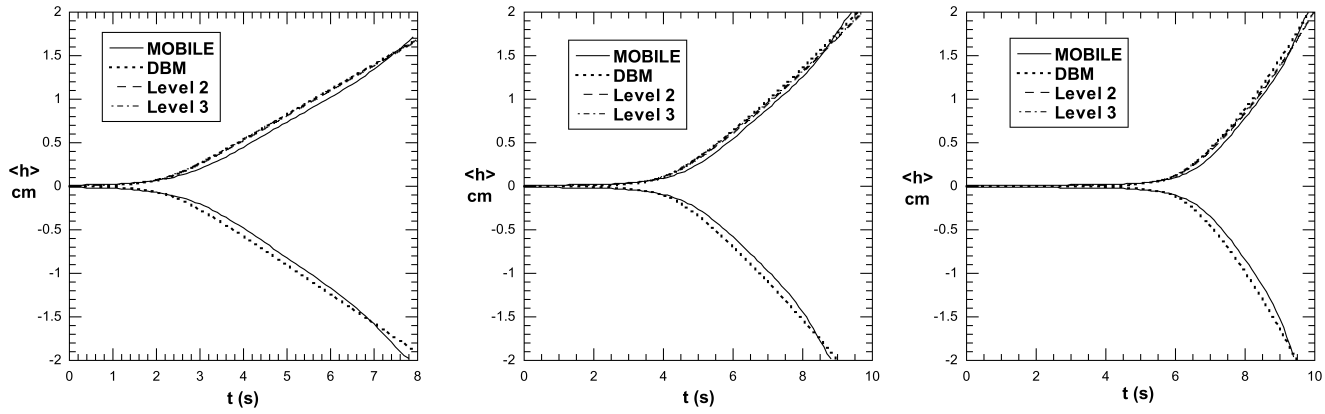


Figure 8 EE11392 15DEC2015

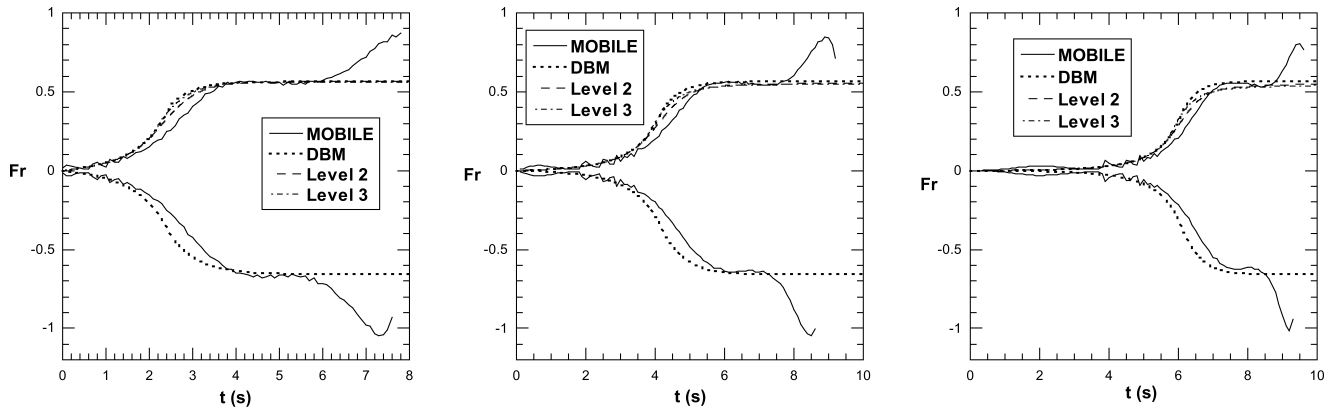


Figure 9 EE11392 15DEC2015

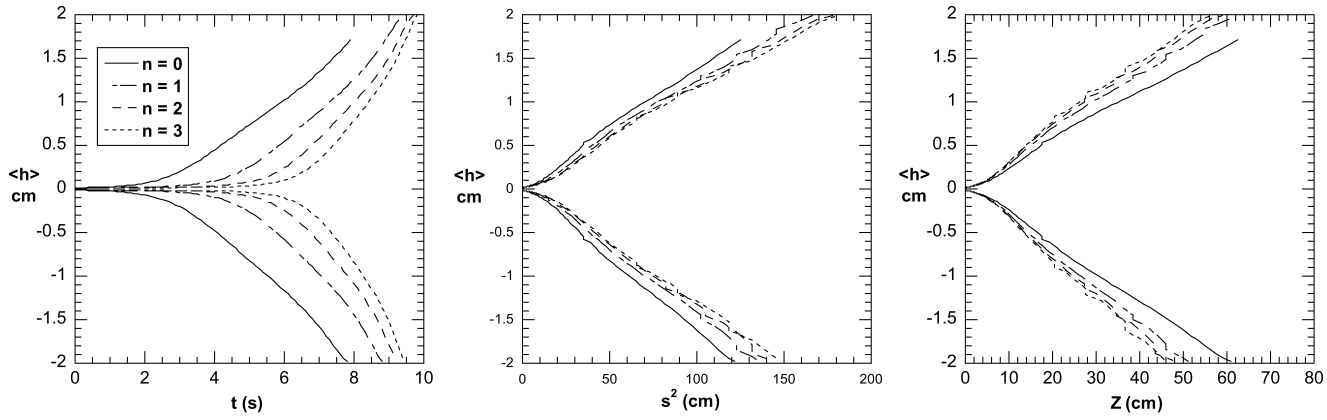


(a) (b) (c)

Figure 10 EE11392 15DEC2015

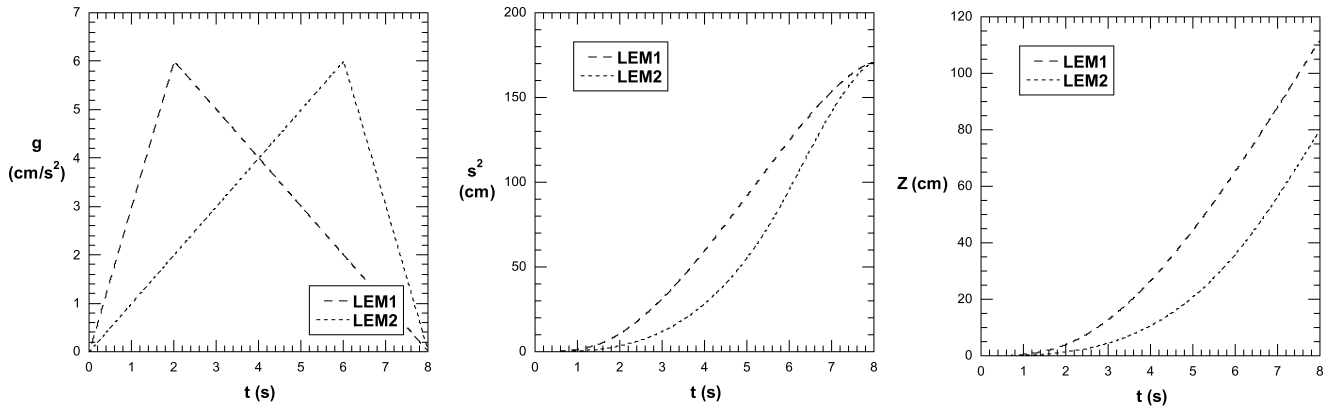


(a) (b) (c)

Figure 11 EE11392 15DEC2015

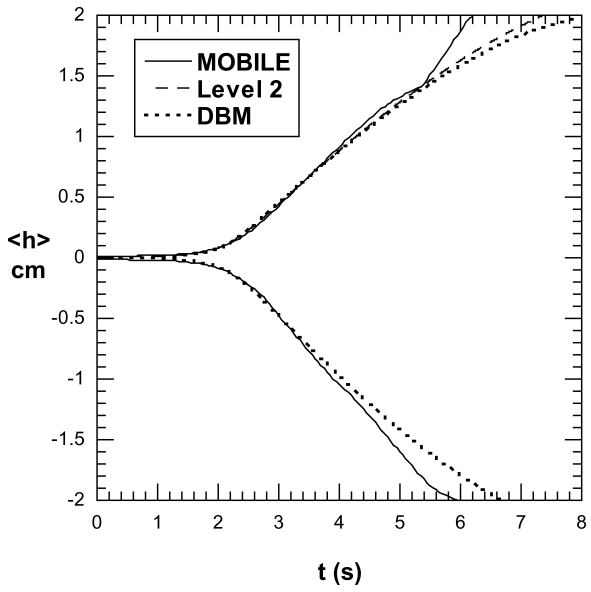


(a)

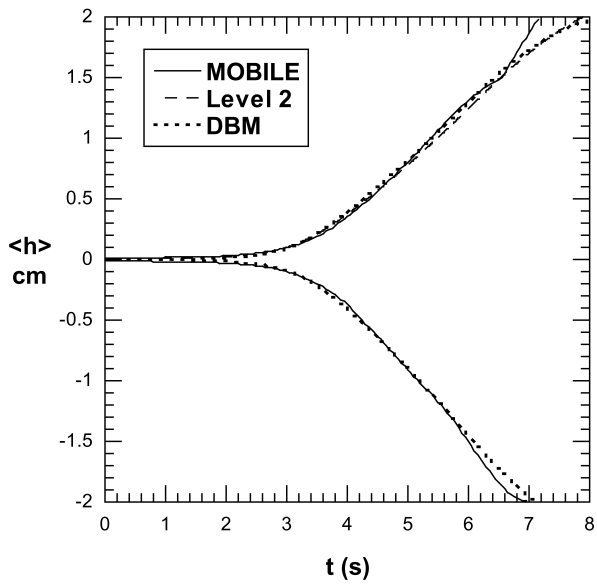


(b)

Figure 12 EE11392 15DEC2015

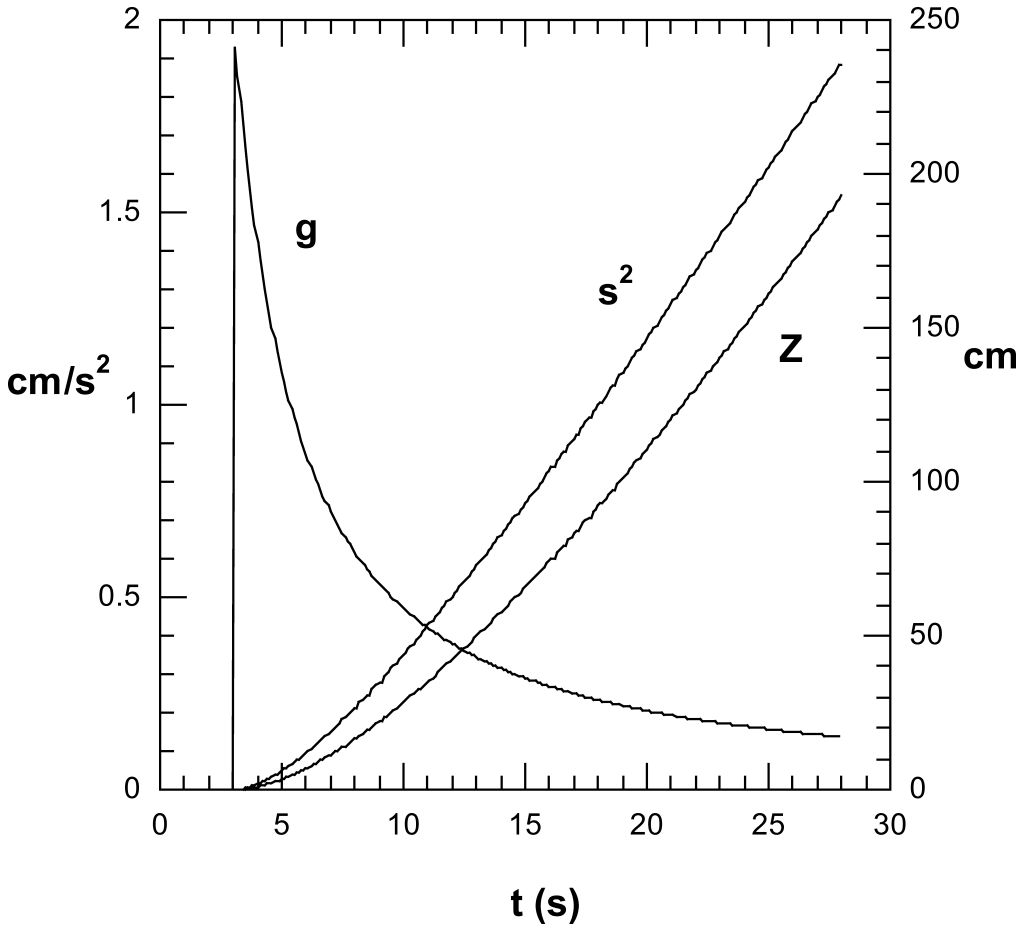


Figure 13 EE11392 15DEC2015

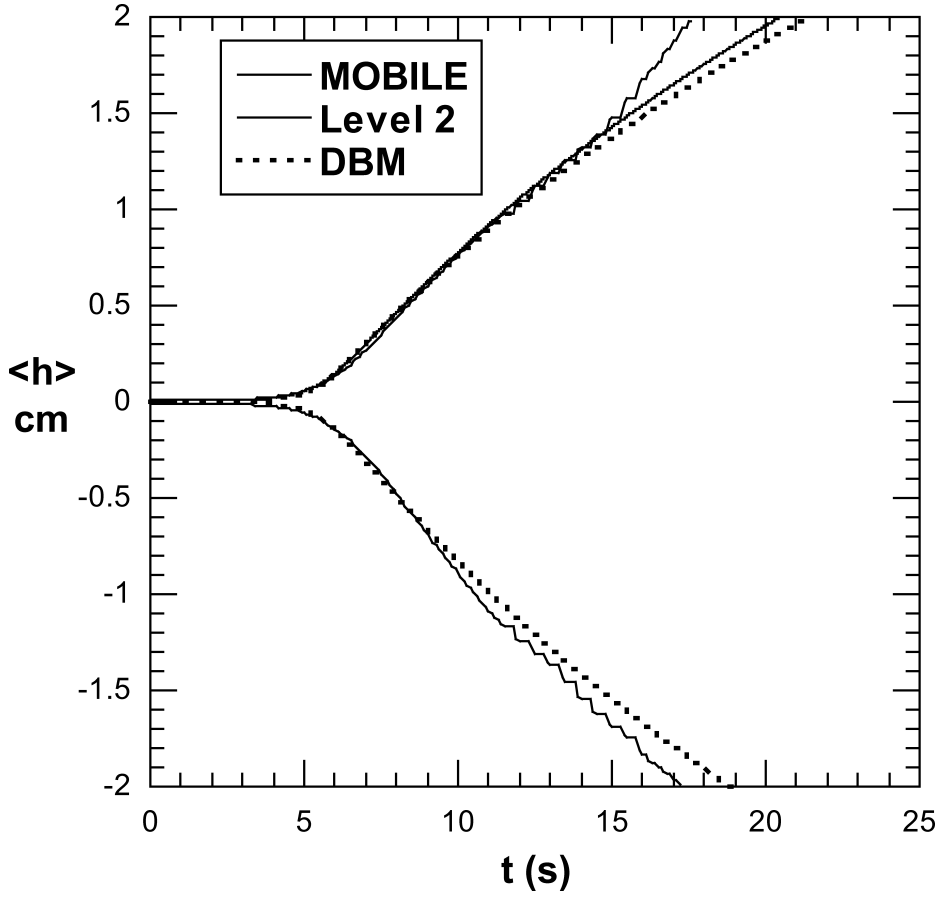


Figure 14 EE11392 15DEC2015

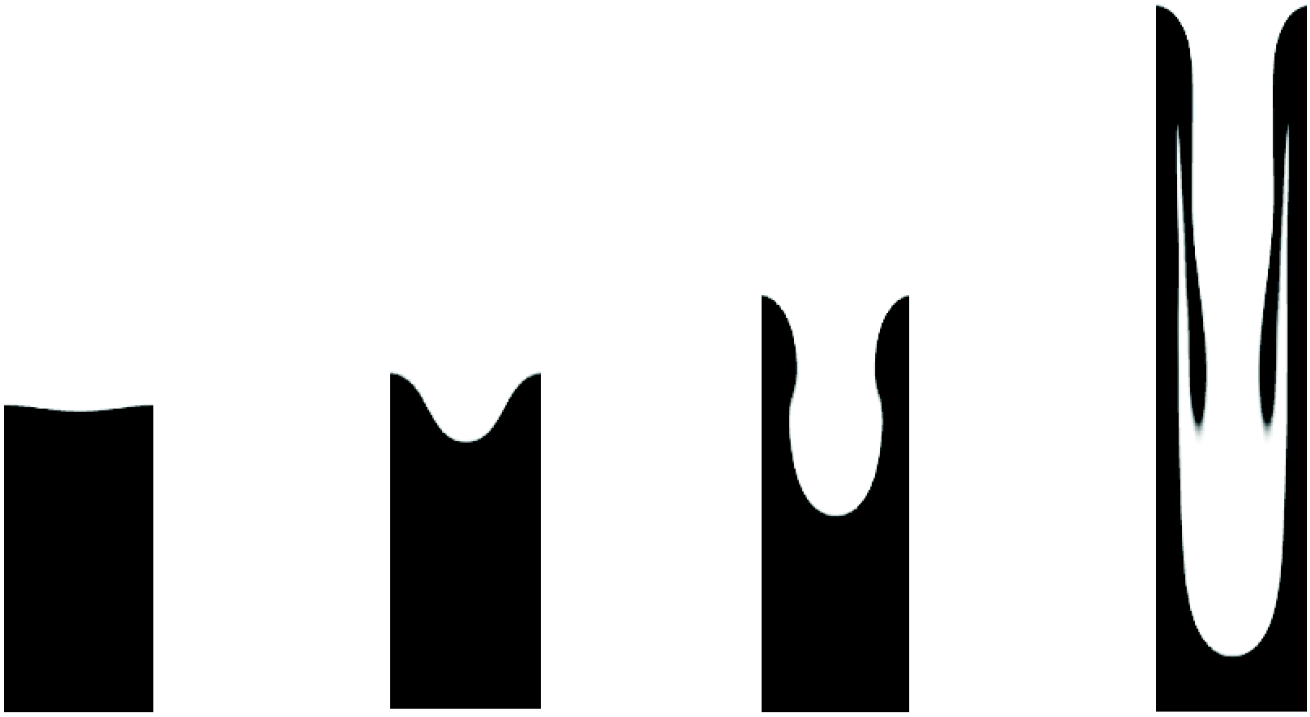


Figure 15 EE11392 15DEC2015

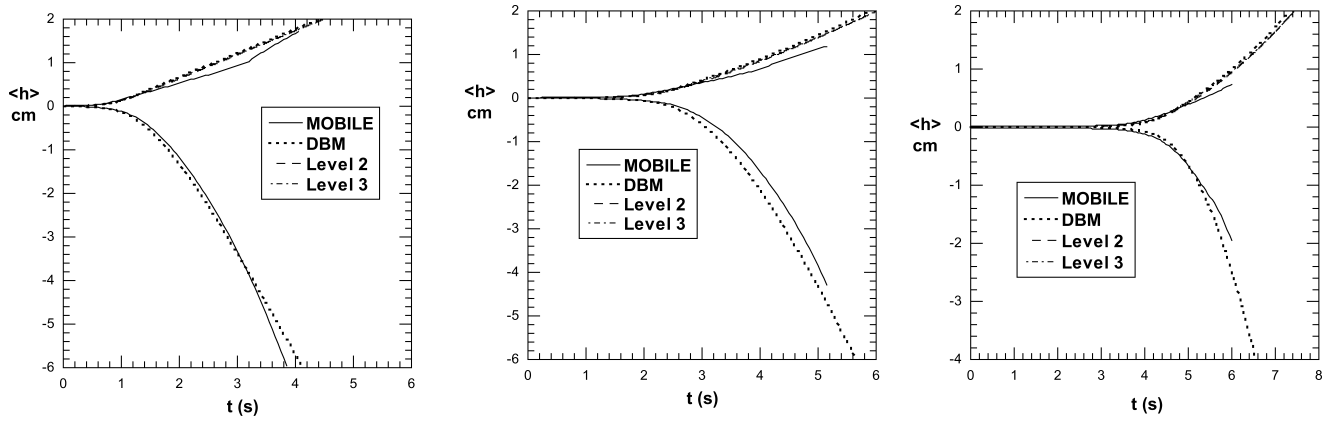


Figure 16 EE11392 15DEC2015

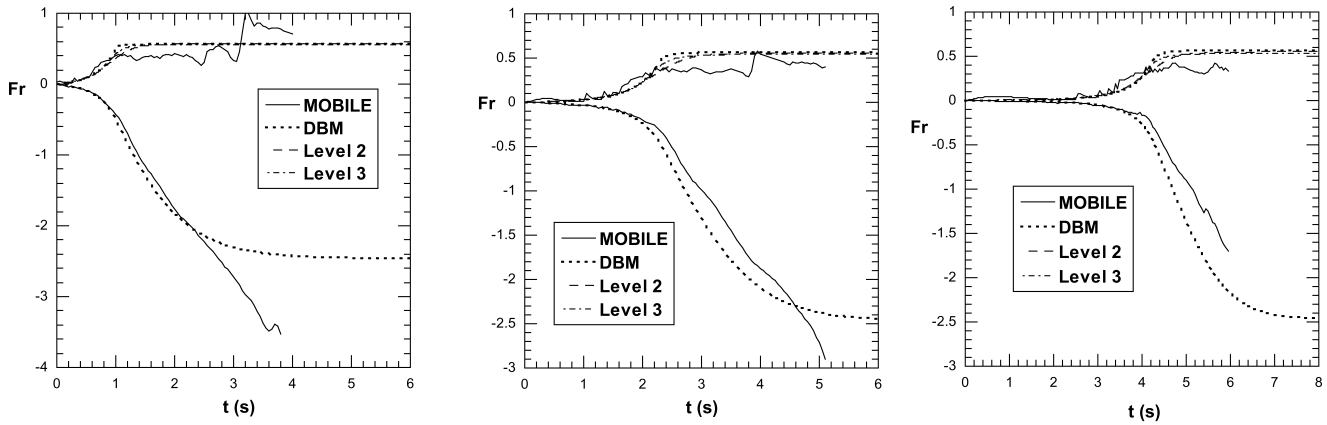


Figure 17 EE11392 15DEC2015

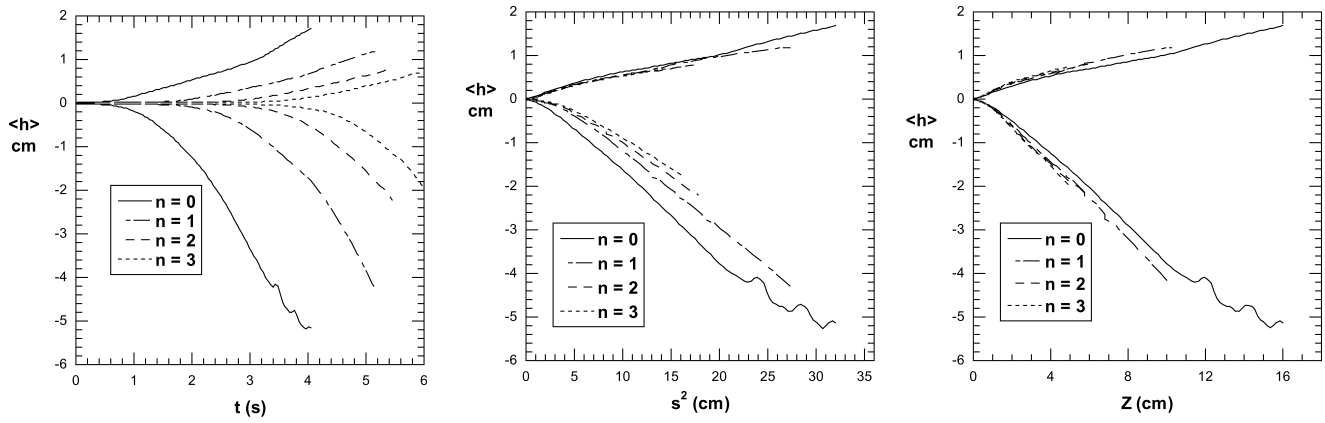


Figure 18 EE11392 15DEC2015

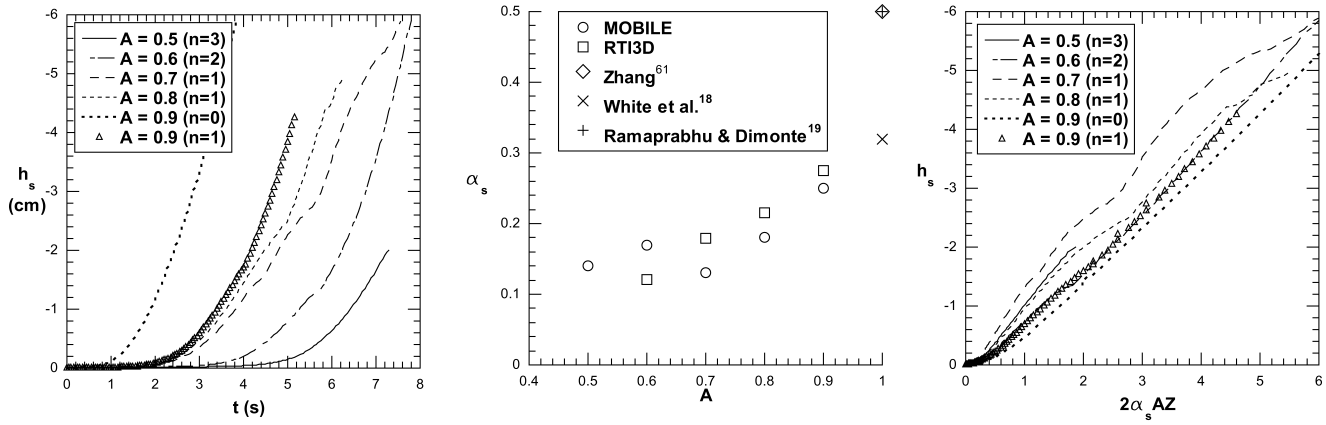


(a) (b) (c)

Figure 19 EE11392 15DEC2015

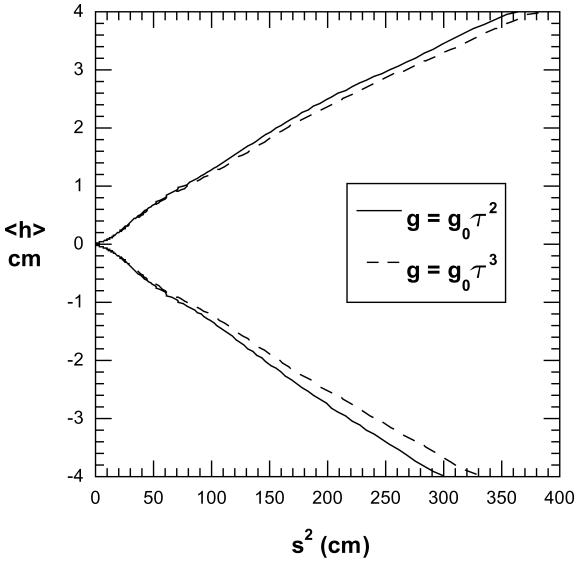


(a)

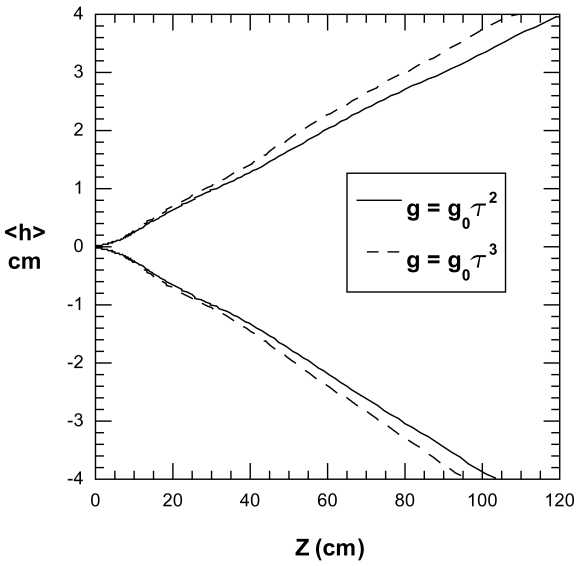


(b)

Figure 20 EE11392 15DEC2015